JOURNAL OF PROPULSION AND POWER
Vol. 27, No. 2, March–April 2011

Experimental and Computational Studies of Low-Temperature Mach 4 Flow Control by Lorentz Force

Munetake Nishihara,* Keisuke Udagawa Takashima,† John R. Bruzzese,‡ and Igor V. Adamovich§
Ohio State University, Columbus, Ohio 43210
and
Datta Gaitonde¶
U.S. Air Force Research Laboratory, Wright-Patterson AFB, Ohio 45433

DOI: 10.2514/1.49243

The paper presents results of cold magnetohydrodynamics flow deceleration experiments using repetitively pulsed, short pulse duration, high-voltage discharge to produce ionization in a $M = 4$ nitrogen flow in the presence of mutually perpendicular dc electric and magnetic fields transverse to the flow. Effective flow conductivity is significantly higher than was previously achieved, $\sigma_{\text{eff}} = 0.1$ S/m, at the magnetic field of 1.5–1.6 T. Magnetohydrodynamics effect on the flow is detected from the flow static pressure measurements. Retarding Lorentz force applied to the flow produces a static pressure increase of 19%, while accelerating force of the same magnitude applied to the same flow results in static pressure increase of 11%. The effect is produced for two possible combinations of the magnetic field and transverse current directions producing the same Lorentz force direction (both for accelerating and retarding force). The results of static pressure measurements are compared with predictions of a 3-D Navier–Stokes/magnetohydrodynamics flow code. The static pressure rise predicted by the code, 20% for the retarding force and 11% for the accelerating force, agrees well with the experimental measurements. The simulations show that at the present conditions, the work done by the accelerating Lorentz force is nearly balanced by Joule heating, resulting in nearly zero net velocity change. On the other hand, the two effects are combined for the retarding Lorentz force, which results in approximately 3.8% flow velocity reduction, by $\Delta u = 25$ m/s. This result provides further evidence of the possibility of cold supersonic flow deceleration by Lorentz force.

Nomenclature

a	=	speed of sound
B	=	magnetic field
C_p, C_c	=	stray capacitances of the capacitive probe
E	=	electric field
e	=	specific total energy
h_D	=	diffuser height
h_T	=	test section height
I	=	current
$\bar{I}$	=	identity tensor
j	=	current density
K	=	loading parameter
L	=	magnetohydrodynamics section length
M	=	flow Mach number
$\dot{m}$	=	mass flow rate
N	=	number density
P	=	pressure
P_0	=	plenum pressure
P_{test}	=	test section static pressure
Pr	=	Prandtl number
Q	=	interaction parameter
q	=	heat flux
R	=	ballast resistance
R_{match}	=	impedance matching resistance
R_{shunt}	=	shunt resistance
R_{term}	=	terminator resistance
R_σ	=	magnetic Reynolds number
Re	=	Reynolds number
T	=	temperature
t	=	time
U_{PS}	=	dc power supply voltage
U_{DC}	=	dc voltage
U_p	=	pulse voltage
$U_{p_{\text{inc}}}$	=	incident pulse voltage
$U_{p_{\text{ref}}}$	=	reflected pulse voltage
U_{scope}	=	voltage signal on the oscilloscope
u	=	flow velocity
W	=	coupled pulse energy
Z_{trans}	=	high-voltage transmission line impedance
Z_{BNC}	=	Bayonet Neill–Concelman cable impedance
α	=	effective Joule heating factor
α_d	=	diffuser step angle
β_s	=	oblique shock angle
γ	=	specific heat ratio
ΔP_R	=	static pressure rise for accelerating Lorentz force
ΔP_R	=	static pressure rise for retarding Lorentz force
μ	=	electron mobility
μ_m	=	magnetic permeability of vacuum
ν	=	pulse repetition frequency
ρ	=	density
σ	=	electrical conductivity
σ_{eff}	=	effective electrical conductivity
τ	=	characteristic time

Presented as Paper 2007-4595 at the 38th AIAA Plasmadynamics and Lasers Conference, Miami, FL, 25–28 June 2007; received 5 February 2010; revision received 2 June 2010; accepted for publication 10 June 2010.

*Postdoctoral Researcher, Nonequilibrium Thermodynamics Laboratories, Department of Mechanical Engineering. Member AIAA.

†Postdoctoral Researcher, Nonequilibrium Thermodynamics Laboratories, Department of Mechanical Engineering. Member AIAA.

‡Graduate Research Associate, Nonequilibrium Thermodynamics Laboratories, Department of Mechanical Engineering. Member AIAA.

§Professor, Nonequilibrium Thermodynamics Laboratories, Department of Mechanical Engineering. Associate Fellow AIAA.

¶Research Aerospace Engineer, Computational Sciences Branch. Fellow AIAA.

$\bar{\tau}$ = shear stress tensor

Subscripts

ref = reference value at the nozzle throat
x, y, z = coordinates

I. Introduction

RECENT experimental studies of low-temperature magnetohydrodynamics (MHD) flows using ionization produced by repetitively pulsed nonequilibrium plasmas demonstrated feasibility of MHD air flow control. In particular, these experiments showed that a retarding Lorentz force results in a density fluctuation increase in a supersonic boundary layer in low-temperature weakly ionized $M = 3$ nitrogen and air flows [1]. Evidence of MHD power extraction was demonstrated in a cold weakly ionized $M = 3$ air flow [2]. Low-temperature weakly ionized $M = 3$ air flow deceleration by the Lorentz force was detected from the flow static pressure measurements [3]. In these experiments, ionization in cold supersonic flows (stagnation temperature $T_0 = 300$ K) was generated by a high-voltage, short pulse duration, high pulse repetition rate discharge, and Faraday current was sustained by transverse dc electric field. Finally, a near-surface dc arc filament discharge in transverse magnetic field was used to delay shock-induced boundary-layer separation in a low-temperature air flow at $M = 2.6$ [4].

The flow deceleration results of [3] are consistent with 3-D compressible Navier–Stokes MHD modeling calculations [5], which suggest that Lorentz force flow acceleration and deceleration may indeed be detected at the flow conductivities realized at the conditions of experiments [1,3]. Specifically, for a $M = 2.6$ nitrogen flow at a stagnation pressure of $P = 1/3$ atm, electrical conductivity of $\sigma = 0.1$ mho/m, magnetic field of $B_z = 1.5$ T, transverse electric field of $E_y = \pm 300$ V/cm, and the MHD section length of $L = 5$ cm, these calculations predict Mach number change by up to $\Delta M = \pm 0.2$. This corresponds to a relative static pressure change of $\Delta P/P = \pm 0.3$, which would be easily detectable in the experiment. Note that in the modeling calculations of [5], Joule heating of the flow by the discharge was neglected, because it is well known that in nonequilibrium nitrogen and air plasmas, direct Joule heating is significantly reduced because a major fraction of the electric discharge power, up to ~90% [6], goes to vibrational excitation of nitrogen. Indeed, effective Joule heating factor, α (i.e., the discharge energy fraction going into Joule heating of the flow), measured in our previous experiments [3] is rather low, $\alpha \sim 0.1$. However, these experiments also demonstrate that Joule heating, although significantly reduced, still remains an important factor affecting the results.

The main objective of the present work is to study the effect of both Joule heating and the Lorentz force on the flow Mach number, determined from static pressure measurements, and to predict this effect using a 3-D compressible Navier–Stokes/MHD flow modeling code. This work follows up on our previous experiments [3] in $M = 3$ nitrogen and air flows by employing a new design of the supersonic test section capable of generating Mach 4 flows, to improve flow quality and reduce the boundary-layer thickness in the test section. Furthermore, the present work considers a more intense MHD interaction obtained using a higher peak voltage and higher pulse repetition rate plasma generator producing higher electrical conductivity of the flow.

II. Description of Experimental Setup

The experiments have been conducted at the supersonic nonequilibrium plasma/MHD blowdown wind-HYPH-tunnel facility described in greater detail in [1,3]. Briefly, this facility generates stable and diffuse supersonic nonequilibrium plasma flows at $M = 3$–4 in a uniform magnetic field up to $B = 2$ T. Figure 1 shows photographs of a supersonic nozzle/MHD test section/diffuser assembly made of transparent acrylic plastic. The assembly consists of a 5.5 cm long converging–diverging nozzle, 12.5 cm long rectangular channel section (including 4.5 cm long electric discharge/MHD section), and 10 cm long diffuser section. The side walls of the MHD section (same as the nozzle contoured walls) diverge at 0.5° each to provide boundary-layer relief. The channel height and width at the MHD section entrance are 40 and 22 mm, respectively. The flow Mach number in the MHD section can be changed between $M = 3$ and $M = 4$ by replacing the nozzle and diffuser inserts shown in Fig. 1.

The MHD test section schematic is shown in Fig. 2. Two rectangular plate copper dc electrodes 4.5 cm long and 2 cm wide, each placed into a boron nitride electrode holder, are flush mounted in the top and bottom walls of the channel. Two pulsed electrode blocks, with a 5 cm × 3.5 cm × 0.3 cm rectangular plate copper electrode sandwiched between mica ceramic blocks and acrylic plastic plates are flush mounted in the side walls, as shown in Fig. 2. The pulsed electrode edges are rounded to achieve a more uniform electric field distribution between the electrodes. The gaps between the pulsed electrodes, the ceramic blocks, and the acrylic plates are filled with silicon rubber to prevent corona formation near the high-voltage electrode surface. The test section is equipped with a stagnation pressure tap in the nozzle plenum and with two static pressure taps located in the side wall, one 4 cm upstream of the dc electrode and the other is 1 cm downstream of the dc electrode. Static pressure in the test section was monitored using a high accuracy Omega PX811-005GAV pressure transducer, at a sampling rate of 67 Hz. Optical access to the test section is provided by four pairs of

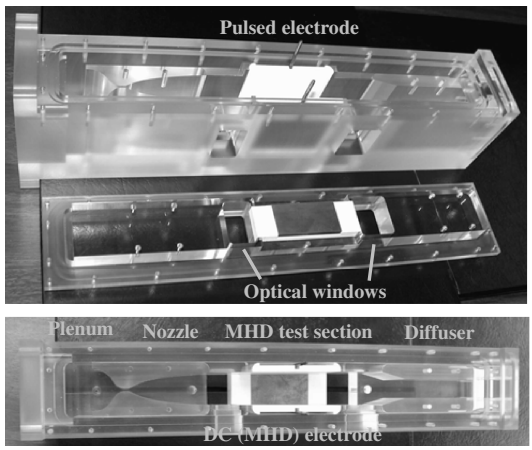

Fig. 1 $M = 4$ supersonic nozzle/pulser-sustainer discharge MHD section/diffuser assembly, shown before diffuser insert geometry adjustment. Flow is from left to right.

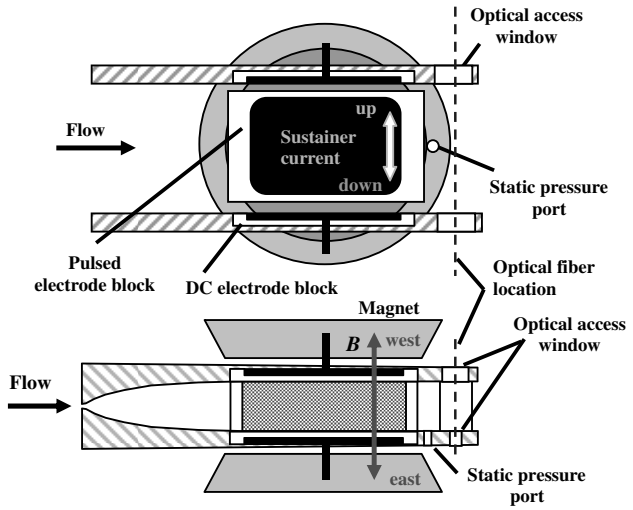

Fig. 2 Schematic of a supersonic nozzle and pulser-sustainer discharge/MHD test section.

rectangular UV grade fused silica windows (Esco Products) placed into the test section walls 1.5 cm upstream and 1.5 cm downstream of the dc electrodes, as shown in Figs. 1 and 2. This allows optical emission measurements along both horizontal and vertical line-of-sight.

The wind tunnel operates using a 1200 ft^3 (34 m^3) dump tank pumped down to 35–40 torr by an Allis-Chalmers 1900 cfm rotary vane vacuum pump. Because of the high back pressure, limited by the vacuum pump cutoff, an angle step diffuser was used downstream of the supersonic test section. The diffuser geometry was determined iteratively, by machining the diffuser inserts to increase the diffuser throat height and to reduce the step angles, until the flow Mach number in the test section, calculated from the static to plenum pressure ratio, became close to the design Mach number. This procedure was used for both $M = 3$ and $M = 4$ diffusers. The resultant ratio of the diffuser height h_D to the supersonic test section height h_T and the diffuser step angle are $h_D/h_T = 0.69$ and $\alpha_d = 6°$ for the $M = 3$ diffuser, and $h_D/h_T = 0.63$ and $\alpha_d = 5°$ for the $M = 4$ diffuser. At these conditions, plenum pressure and test section static pressure for the $M = 3$ nozzle/diffuser are $P_0 = 250$ torr and $P_{\text{test}} = 9$ torr, and those for the $M = 4$ nozzle/diffuser are $P_0 = 600$ torr and $P_{\text{test}} = 4.8$ torr. This corresponds to the flow Mach number of $M = 2.80$ and $M = 3.85$, respectively. The nozzle throat dimensions are 40 mm × 4.8 mm for the $M = 3$ nozzle and 40 mm × 1.8 mm for the $M = 4$ nozzle, which gives mass flow rates of $\dot{m} = 15$ g/s and $\dot{m} = 14$ g/s, respectively. The entire nozzle/test section/diffuser assembly is placed between the poles of a GMW water cooled electromagnet. In the present experiments, for the 6.5 cm distance between the 15 cm diameter poles, the magnetic field at maximum current through the magnet coils of 140 A is $B = 1.63$ T. The magnetic field generated by the electromagnet with 15 cm diameter poles and 6.5 cm pole separation remains nearly constant across the discharge section 4.5 cm long (within about 10%). A 10 mm diameter circular hole drilled in the center of each magnet pole provides optical access to the test section through the side walls fused silica windows. The magnetic field direction can be switched by changing the magnet power supply polarity. In the present work, two transverse magnetic field directions are referred to as east and west, respectively, (see Fig. 2).

A high-voltage, short pulse duration, high-repetition rate pulse generator (fast ionization dynistor, or FID, GmbH, FPG 60-100MC4) is used to produce ionization in the test section. The pulse generator produces high-voltage, nanosecond duration pulses (peak voltage 8 kV, pulse duration 4 nsec full width at half maximum, FWHM) at a pulse repetition of up to 100 kHz using fast semiconductor switches, Fast Ionization Dynistors [7]. The pulser has four high-voltage output channels, two of them positive polarity and the other two negative polarity. In the present work, the pulser is operated in two different modes, two-channel and four-channel. The first mode is using two output channels (one positive and one negative) connected to the pulsed electrodes in the MHD section by two 3 m long, 75 Ω coaxial transmission cables, so that two opposite polarity pulses (+8 kV and −8 kV) are sent to the load simultaneously, thereby doubling the incident pulse voltage on the electrodes. In the second mode, four output channels are connected to a four 75 Ω cable assembly, in which the central wire of one positive polarity cable is connected to the shielding of the other positive polarity cable before the load, and the same connection is used for the negative polarity cables. This connection doubles both the positive and the negative voltage pulse amplitude (to +16 kV and −16 kV, respectively), so that the incident pulse voltage on the electrodes is quadrupled. Note that the actual peak voltage between the electrodes may be significantly higher than 16 and 32 kV for the two-channel and four-channel modes, respectively, because of the incident pulse reflection. In the absence of the load (i.e., when the cables are disconnected from the pulsed electrodes and therefore the entire high-voltage pulse is reflected), the positive-to-negative voltage at the end of the transmission cables is 32 and 64 kV, respectively.

Transverse dc current (sustainer current) in the supersonic flow ionized by the repetitively pulsed discharge is sustained by applying a dc field (up to 500 V/cm) to two dc electrodes flush mounted in the top and bottom nozzle walls, perpendicular both to the flow velocity and to the magnetic field direction, as shown in Fig. 2. The transverse dc field is applied using a DEL 2 kV/3 A power supply operated in a voltage stabilized mode, with a 0.5 kΩ ballast resistor. Two inductors 1 mH each are placed in the dc circuit in series with both dc electrodes to attenuate high amplitude current pulses propagating into the dc circuit. Current in the dc sustainer circuit is measured using a Tektronix AM503S current probe. The dc current direction (referred to as "up" and "down" in the present work, see Fig. 2) can be changed by switching the power supply polarity.

As discussed in our previous work [3], generation of decelerating and accelerating Lorentz force using two combinations of current and magnetic field vectors for each is essential to isolate the work done by the Lorentz force from the Joule heating effect. If the Lorentz force interaction indeed results in significant flow acceleration, the flow static pressure would decrease for both **j** and **B** vectors configurations producing an accelerating Lorentz force and increase for the other two configurations producing a retarding Lorentz force. On the other hand, if the electric discharge power at these conditions remains the same, Joule heating would result in a static pressure increase (i.e., Mach number reduction), which would be the same for all four of these cases. In the case when both these factors, Lorentz force and Joule heating, generate comparable effects on the flow, the static pressure dependence on the Lorentz force direction should still be apparent.

In the present work, nanosecond pulse voltage is measured by two different methods, using a back current shunt probe [8] and a capacitive probe [9–11]. The schematics of the two probes are shown in Figs. 3 and 4. Both probes are installed 1.3 m from the load in one of a 3 m long transmission cables, to avoid an overlap of an incident pulse generated by the pulser and a pulse reflected from the load. In the current shunt, twelve low inductance, low capacitance 3 Ω resistors (Xicon SMD chip resistors) are placed in the 1 cm gap cut in the cable shielding, along the circumference of the dielectric material separating the center wire and the shielding of the cable. The total resistance of the shunt is therefore $R_{\text{shunt}} = 0.25$ Ω. When a high-voltage pulse $U_p(t)$ propagates through the transmission cable, current pulses of the same magnitude, $I(t) = U_p(t)/Z_{\text{trans}}$, propagate in the opposite directions through the central wire and the shielding. Here $Z_{\text{trans}} = 75$ Ω is the transmission cable impedance. The voltage drop on the shunt is measured using a BNC coaxial cable ($Z_{\text{BNC}} = 50$ Ω) connected in series with a $R_{\text{match}} = 49.8$ Ω impedance matching resistor (Xicon SMD chip) and with a Lecroy Wavepro 7100 A, 1 GHz bandwidth oscilloscope with a $R_{\text{term}} = 50$ Ω terminator, as shown in Fig. 3. This resistive voltage divider circuit helps avoiding voltage pulse reflections both at the terminator and at the shunt. The pulse voltage in the transmission line is calculated as follows

$$U_p(t) = \frac{Z_{\text{BNC}} + R_{\text{match}}}{Z_{\text{BNC}}} \frac{Z_{\text{trans}}}{R_{\text{shunt}}} U_{\text{scope}}(t) \tag{1}$$

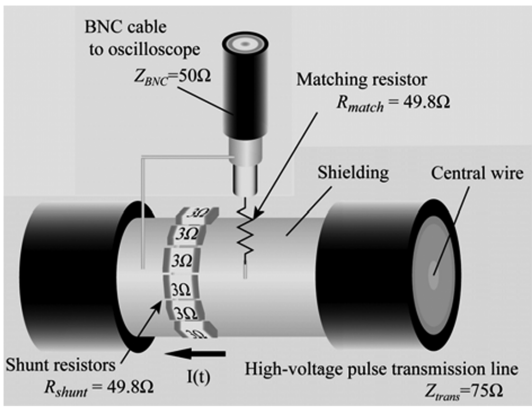

Fig. 3 Schematic of a back current shunt.

where $U_{\text{scope}}(t)$ is a voltage signal on the oscilloscope, i.e., the pulse voltage is attenuated by a factor of 600. The current shunt was calibrated using a 250 V amplitude, 10 nsec rise time rectangular voltage pulse generated by a custom-made calibration pulse generator.

Figure 4 shows a schematic and an equivalent circuit of the capacitive probe, which operates as a capacitive voltage divider circuit. The feedthrough capacitor is custom made of a 1.5 mm × 1.5 mm square copper plate (contact surface) soldered to the tip of a copper wire (central wire of a 50 Ω BNC coaxial cable), insulated by a multilayer piece of Kapton tape 1 cm wide wrapped around it, and covered with a copper tape sleeve soldered to the shield line of the BNC cable, as shown in Fig. 4. The capacitor is placed into a channel cut in the dielectric material between the central wire and the shielding of the 75 Ω high-voltage pulse transmission cable, as shown in Fig. 4. The distance from the central wire of the transmission cable to the contact surface is approximately 1 mm. Stray capacitances between the contact surface and the central wire, C_p, and between the contact surface and the shielding, C_c, such that $C_c \gg C_p$, are shown in Fig. 4. The BNC cable, in series with a $R_{\text{match}} = 49.8\ \Omega$ impedance matching resistor, is connected to the oscilloscope through a terminator, $R_{\text{term}} = 50\ \Omega$. When a high-voltage pulse propagating along the transmission cable arrives at the location of the contact surface, the stray capacitors first charge and then discharge through the terminator. The pulse voltage is determined from the voltage on the capacitor C_c, measured by the oscilloscope, as follows [9]:

$$U_p(t) = A\frac{Z_{\text{BNC}} + R_{\text{match}}}{Z_{\text{BNC}}}\left(U_{\text{scope}}(t) + \frac{1}{\tau}\int_0^t U_{\text{scope}}(t')\mathrm{d}t'\right) \tag{2}$$

where

$$\tau = (Z_{\text{BNC}} + R_{\text{match}})(C_c + C_p) \qquad A = \frac{C_p + C_c}{C_p} \tag{3}$$

are the resistance-capacitance circuit time constant and the voltage divider circuit coefficient. Their values, $\tau = 0.26$ ns and $A = 100$, have been determined from calibration using the same 250 V, 10 nsec rise time calibration pulse.

Flow temperature downstream of the MHD test section was inferred from the nitrogen second positive band emission spectra taken using a 5 m long optical fiber (BFL22-200, Thor Labs) with collimators at each end, and a Princeton Instruments Optical Multichannel Analyzer with a 0.5 m monochromator, 1200 lines/mm grating, and an intensified charge-coupled device camera. Field of view of the optical fiber was mapped using a point light source (∼0.2 mm aperture), which showed the signal collection region to be a cylinder 2–3 mm in diameter and at least 50 mm long, with signal contribution along the line of sight being very nearly constant. Therefore, for a vertical line-of-sight emission measurement, the signal collection region incorporates both the supersonic core flow and the boundary layers downstream of dc electrodes, while for a horizontal line-of-sight measurement, the signal is collected from the supersonic core flow and from the boundary layers downstream of the pulsed electrodes. Rotational temperature of the flow was inferred using a synthetic spectrum [3] with the accurate nitrogen molecular constants, rotational like intensities, and the experimentally measured slit function of the spectrometer.

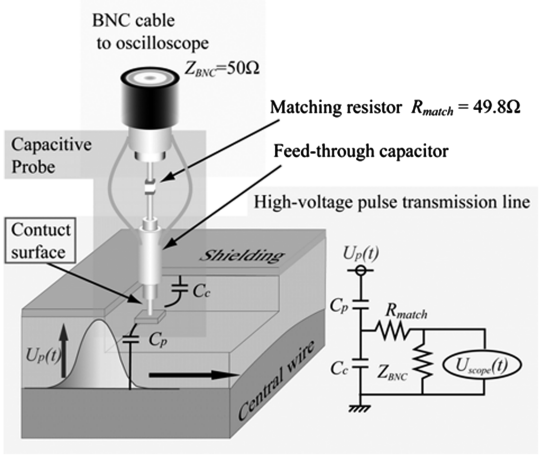

Fig. 4 Schematic and an equivalent circuit of a capacitive probe.

III. Numerical Model

In the present work, numerical simulation of the flow in the supersonic nozzle, MHD test section, and the diffuser was performed using a 3-D compressible Navier–Stokes/MHD flow code described in detail in [12,13]. At low magnetic Reynolds numbers, the induced magnetic field is negligible, and the governing equations are obtained by adding the Lorentz force term to the momentum equation, as well as the Joule heating term to the total energy equation in the Navier–Stokes equations [12]

$$\frac{\partial \rho}{\partial t} + \nabla \cdot (\rho \mathbf{u}) = 0 \tag{4}$$

$$\frac{\partial \rho \mathbf{u}}{\partial t} + \nabla \cdot [\rho \mathbf{u}\vec{u} + P\bar{I}] - \frac{1}{Re}\nabla \cdot \bar{\tau} = Q(\mathbf{j} \times \mathbf{B}) \tag{5}$$

$$\frac{\partial \rho e}{\partial t} + \nabla \cdot \left[(\rho e + P)\mathbf{u} - \frac{1}{Re}(\mathbf{u} \cdot \bar{\tau}) - \frac{1}{(\gamma - 1)PrM^2Re}\mathbf{q}\right] = Q[\alpha(\mathbf{E} \cdot \mathbf{j}) + (1 - \alpha)\mathbf{u}(\mathbf{j} \times \vec{B})] \tag{6}$$

$$e = \frac{P}{(\gamma - 1)\rho} + \frac{\mathbf{u}^2}{2} \tag{7}$$

where t is the time, ρ is the density, $\mathbf{u}$ is the velocity vector, P is the pressure, $\mathbf{B}$ and $\mathbf{E}$ are the magnetic and the electric fields, respectively, $\mathbf{j}$ is the current density, $\bar{I}$ and $\bar{\tau}$ are identity and shear stress tensors, respectively, $\mathbf{q}$ is the heat flux vector, e is the total energy per unit mass, and α is the effective Joule heating factor (the discharge energy fraction going into Joule heating of the flow) [3]. The nondimensional parameters are the Reynolds number, Re, the Prandtl number, Pr, the Mach number, M, and the interaction parameter $Q = \sigma_{\text{ref}} B_{\text{ref}}^2 L_{\text{ref}}/(\rho_{\text{ref}} U_{\text{ref}})$, where σ_{ref} is the electrical conductivity, B_{ref} is the externally applied magnetic field, and L_{ref} is the reference length (nozzle throat height). The rest of the reference parameters are parameters at the nozzle throat. At the present conditions ($L_{\text{ref}} = 0.18$ cm, $U_{\text{ref}} = 316$ m/s, $\sigma_{\text{ref}} = 0.17$ mho/m), the magnetic Reynolds number is $R_\sigma = \mu_m L_{\text{ref}} U_{\text{ref}} \sigma_{\text{ref}} \sim 10^{-7} \ll 1$ (here μ_m is the magnetic permeability of vacuum), and the magnetic field is assumed to be constant and equal to the externally applied field. The current density and the electric field are found from the generalized Ohm's law neglecting ion slip [12]

$$\mathbf{j} = \sigma[\mathbf{E} + \mathbf{u} \times \mathbf{B}] - \frac{\beta}{|\mathbf{B}|}(\mathbf{j} \times \mathbf{B}) \tag{8}$$

and from the current continuity equation

$$\nabla \cdot \mathbf{j} = 0 \tag{9}$$

In Eq. (8), σ is the scalar electric conductivity of the flow and $\beta = \mu B$ is the electron Hall parameter, where μ is the electron mobility, $\mu = 0.147 \cdot \mathrm{T(K)/P(torr)m^2/V \cdot s}$ [14]. In the present work, the Hall parameter was calculated at $T = 80$ K, $P = 5$ torr, and $B = 1.5$ T, and assumed to be constant, $\beta = 3.5$, in the entire $M = 4$ test section. The conductivity, which was assumed to be constant in the region between the pulser electrodes, was adjusted until the calculated current agreed with the experimental value at the same

voltage between the dc electrodes. The present approach somewhat underestimates the flow conductivity because it neglects the cathode voltage fall [14].

The computational domain extends from the nozzle throat, where the flow is assumed to be uniform at $M = 1$, to the end of the supersonic section, where zero axial gradient boundary conditions are imposed. The wall boundary conditions are no-slip, zero pressure gradient, and constant wall temperature ($T = 300$ K) conditions. The number of mesh points in the flow direction (x), magnetic field direction (y), and electric field direction (z) is 151, 61, and 51, respectively. Initial conditions are obtained from a quasi-one-dimensional isentropic expansion flow based on the area ratio. The system of Eqs. (4–9) is solved using a first-order Beam-–Warming method with third-order upwind-biased Roe-averaged fluxes with a harmonic limiter, until steady state is reached. Detailed discussion of time-marching strategy and spatial differencing scheme can be found in [12] and references therein.

IV. Results and Discussion

Figure 5 shows a photograph and a schematic of the oblique shock system in the $M = 4$ diffuser section visualized by the high-voltage repetitively pulsed discharge generated in the MHD section. In the present experiments, the pulser-sustainer discharge appears diffuse and volume filling. However, somewhat brighter emission is observed near the side walls (top and bottom walls in the photograph), i.e., close to the pulsed electrodes, and in the center of the test section. Note that the oblique shocks do not extend through the boundary layer to the test section walls. A linear extrapolation of the shock fronts suggests that the oblique shocks originate somewhat upstream of the 5.5° diffuser step angles, possibly due to flow separation at the compression corners. The oblique shock wave angle determined from the photograph is approximately $\beta_s = 19°$, which corresponds to the flow Mach number at the end of the test section of $M = 3.85$. This is consistent with the static pressure measurements 1 cm downstream of the MHD section, $P = 4.8$ torr for the stagnation pressure of $P_0 = 600$ torr, which also corresponds to $M = 3.85$.

Figure 6 shows incident and reflected high-voltage pulses for a single pulse generated during the two-channel pulser operation at atmospheric pressure in the test section, measured by the capacitive probe and by the current shunt, discussed in Sec. II. At these conditions, there is no breakdown in the test section, so that the entire pulse is reflected. Incident pulse peak voltages (at $t = 30$ nsec) measured by the capacitive probe and by the current shunt are 8.1 and 8.3 kV, respectively, while reflected pulse peak voltages (at 50 nsec) are 7.0 and 8.0 kV, respectively. Although the peak incident pulse voltage measured by the capacitive probe is somewhat lower than that measured by the current shunt, both measurements resulted in almost the same FWHM of 4.2 ns, rise time of 1.6 ns, and fall time of 1.8 ns. Estimated pulse energy coupled to the load (which should be zero at these conditions) was calculated as the difference of the incident and the reflected pulse energies [15]

$$W = \int \frac{U_{p_{\text{inc}}}(t)^2}{Z_{\text{trans}}}\,\mathrm{d}t - \int \frac{U_{p_{\text{ref}}}(t)^2}{Z_{\text{trans}}}\,\mathrm{d}t \tag{10}$$

0.5 mJ/channel based on the capacitive probe signal and 0.3 mJ/channel based on the current shunt probe signal. In Eq. (10), $Z_{\text{trans}} = 75\ \Omega$ is the transmission cable impedance. Both numbers are close to each other and are much lower than the incident pulse energy, 3.1 mJ. Note that this result provides an estimate of the uncertainty in the coupled pulse energy measurement. The capacitive probe bandwidth, estimated using the same method as in [9], is ~20 GHz, above which the inductance of the feedthrough capacitor may affect the signal. On the other hand, reactivity of chip resistors used in the current shunt starts affecting the signal at a significantly lower frequency, of the order of 1 GHz. Also, the reflected pulse measured by the current shunt at the conditions when plasma was generated between the electrodes was very noisy. Because of this, we used the capacitive probe for further incident and reflected pulse energy measurements.

Figure 7 shows incident and reflected pulses measured by the capacitive probe with a two-channel pulsed discharge operated in the test section at a pulse repetition rate of $\nu = 100$ kHz, for the 1st pulse and for the 4000th pulse (i.e., 40 ms later). These measurements are taken with the pulsed discharge operated in a $M = 4$ nitrogen flow at $P_0 = 600$ torr, $P_{\text{test}} = 4.8$ torr, and $B = 1.63$ T. It can be seen that the incident pulse peak voltage is 8.1 kV for the 1st pulse and 7.0 kV for the 4000th pulse. The reflected pulse voltage for the 4000th pulse is also reduced compared with the 1st pulse (see Fig. 7). The pulse voltage decrease may be due to residual charge accumulation in the transmission cable and on the dielectric plates covering the pulsed electrodes. Pulse energy coupled to the plasma, calculated from the waveforms of Fig. 7, is 1.1 mJ/channel for the 1st pulse and 0.6 mJ/channel for the 4000th pulse. This corresponds to 60 W/channel time-averaged discharge power at $\nu = 100$ kHz at the steady state conditions (i.e., 240 W for the four-channel operation). However, note that because the coupled pulse energies are rather low and comparable with the coupled pulse energy measured in the absence of the plasma (0.5 mJ/channel), this result has a large uncertainty and could be significantly lower. Basically, these measurements suggest even when a plasma is sustained between the pulsed electrodes, most of the incident pulse energy (at least 80%) is reflected. For comparison, in our previous coupled pulse energy measurements in a $M = 3$ nitrogen flow at $B = 1.5$ T [3] using a chemical physics technologies (CPT) nanosecond pulse generator (peak voltage 13–15 kV, pulse duration 30 ns, pulse repetition rate $\nu = 40$ kHz),

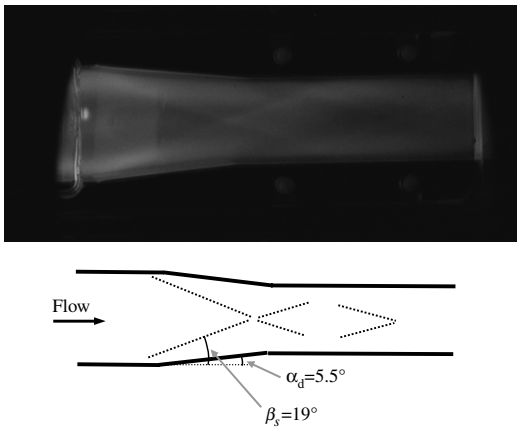

Fig. 5 Photograph and schematic of an oblique shock pattern in the $M = 4$ diffuser. Nitrogen, $P_0 = 600$ torr, $P_{\text{test}} = 4.8$ torr ($M = 3.85$).

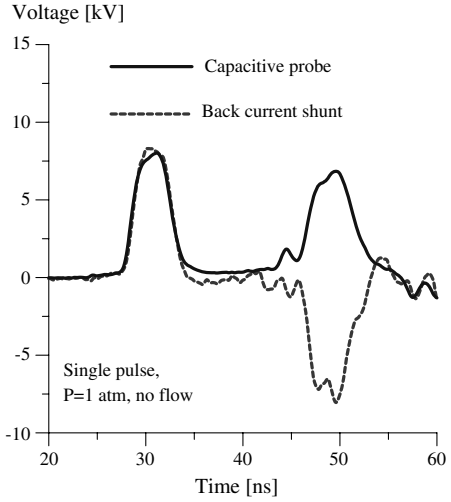

Fig. 6 Incident and reflected pulse voltage waveforms measured by the capacitive probe and by the back current shunt at atmospheric pressure (no breakdown) in the test section.

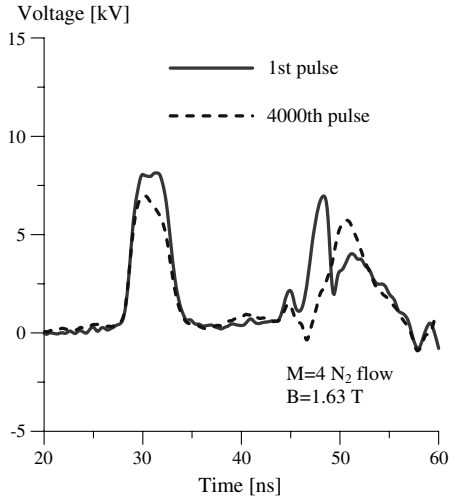

Fig. 7 Incident and reflected voltage pulses measured by the capacitive probe for the 1st pulse and for the 4000th pulse. $M = 4$ nitrogen flow, $P_{\text{test}} = 4.8$ torr, $B = 1.63$ T, $\nu = 100$ kHz.

coupled pulse energy was 1–2 mJ and the time-averaged discharge power was 40–80 W.

Figure 8 shows oscillograms of dc sustainer current in a $M = 4$ nitrogen flow at $P_0 = 600$ torr, $P_{\text{test}} = 4.8$ torr, and $B = 1.63$ T, ionized by a $\nu = 100$ kHz four-channel pulsed discharge. In Fig. 8, dc power supply voltage is $U_{\text{PS}} = \pm 1.4$ kV and a ballast resistance is $R = 0.5$ kΩ. It can be seen that the sustainer current peaks at $I = 1.2$ A approximately 3 μs after each ionizing pulse, and decays to $I = 0.75$ A before the next pulse. For both dc voltage polarities, the time-averaged sustainer currents are very close, $\langle I \rangle = 0.94$ A and 0.93 A, respectively. This corresponds to the time-averaged voltage between the electrodes, $\langle U \rangle = U_{\text{PS}} - \langle I \rangle R = 0.93$ kV and the dc discharge power of 0.87 kW. For comparison, in our previous measurements in $M = 3$ nitrogen and air flows [3], ionized by the CPT pulser at $\nu = 40$ kHz, the dc discharge current, voltage and power were $\langle I \rangle = 0.9$ A, $\langle U \rangle = 1.6$ kV, and 1.4 kW, respectively. It can be seen that flow ionization by the FID pulser operated in the four-channel mode produces comparable sustainer currents at significantly lower dc voltages, i.e., the FID pulser generates higher flow conductivity.

This effect is further illustrated by comparing current-voltage characteristics of the sustainer discharge for the two-channel and four-channel operation modes $\nu = 100$ kHz in a $M = 4$ nitrogen flow, and for the CPT pulser in a ionized by the CPT pulser (0 kHz) [1], both measured in magnetic field of $B = 1.5$ T (see Fig. 9). The effective electrical conductivities for these two cases were determined from linear fits to the current-voltage characteristics, as shown in Fig. 9, $\sigma_{\text{eff}} = 0.04$ S/m for the $M = 3$ flow/CPT pulser, and $\sigma_{\text{eff}} = 0.1$ S/m for the $M = 4$ flow/four-channel FID pulser. We conclude that the flow conductivity generated by the FID pulser is indeed significantly higher, by about a factor of 2.5. Note that the scalar flow conductivity, i.e., the conductivity measured at $B = 0$, is higher [1], because in the presence of magnetic field the conductivity is reduced due to the Hall effect.

Figure 10 shows plasma visible emission spectra, $1 \rightarrow 4$ band of nitrogen second positive system ($C^3\Pi_u \rightarrow B^3\Pi_g$), averaged along the horizontal line-of-sight by the optical fiber, taken in the repetitively pulsed discharge with and without dc voltage applied. The flow conditions in Fig. 10 are nitrogen at $P_0 = 600$ torr, $P_{\text{test}} = 4.8$ torr, $B = 1.5$ T, with a four-channel pulsed discharge operating at $\nu = 100$ kHz. The dc power supply voltage was $U_{\text{PS}} = 1.3$ kV. It can be seen that the two spectra are very close to each other, suggesting that flow temperature increase due to the dc discharge is small. As discussed in our previous work [3], at the

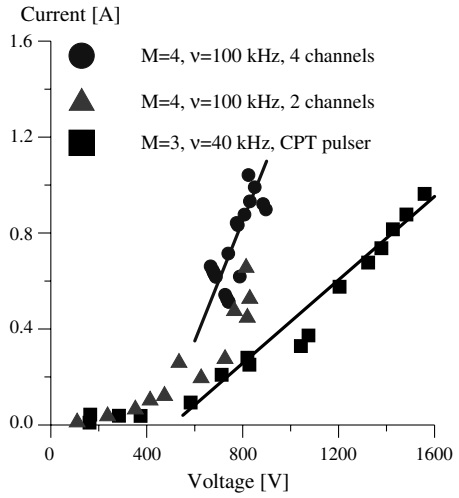

Fig. 9 Current voltage characteristics in nitrogen flows at $B = 1.5$ T, for different Mach numbers and different pulser operation modes. For $M = 3$, $P_0 = 250$ torr, $P_{\text{test}} = 7.5$ torr, $\nu = 40$ kHz [3]. For $M = 4$, $P_0 = 600$ torr, $P_{\text{test}} = 4.8$ torr, $\nu = 100$ kHz.

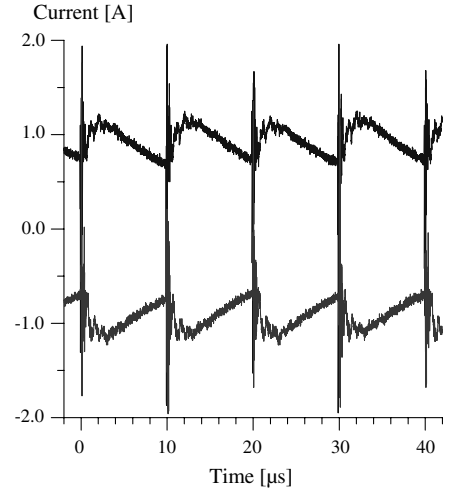

Fig. 8 Sustainer discharge current traces for two different transverse dc electric field polarities. M=4 nitrogen flow, $P_0 = 600$ torr, $P_{\text{test}} = 4.8$ torr, $B = 1.5$ T, $\nu = 100$ kHz, $U_{\text{PS}} = 1.4$ kV, $R = 0.5$ kΩ. Time-averaged currents are 0.94 A (top curve) and 0.93 A (bottom curve).

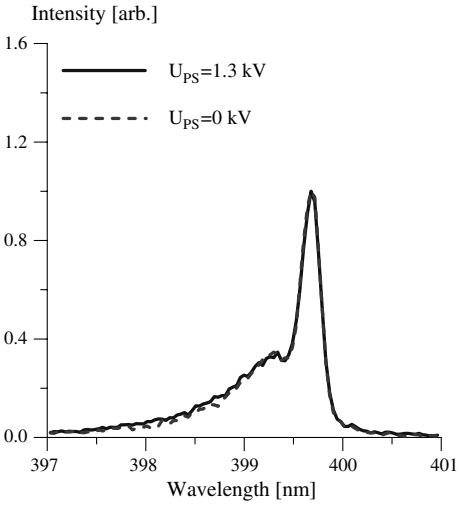

Fig. 10 $N_2(C^3\Pi_u \rightarrow B^3\Pi_g)$ emission spectra ($1 \rightarrow 4$ band) measured along a horizontal line-of-sight in a $M = 4$ nitrogen flow at $P_0 = 600$ torr, $B = 1.5$ T, and $\nu = 100$ kHz, with and without 0.9 kW dc sustainer discharge.

reduced electric field in the sustainer discharge, $E/N = (3\text{–}4) \cdot 10^{-16}$ V · cm^2 (based on the isentropic core flow temperature estimated from the quasi-one-dimensional flow theory), most of the discharge energy, up to 90%, goes to vibrational excitation of nitrogen and remains "locked" there due to its slow vibrational relaxation. Figure 11 compares the experimental spectrum without dc voltage applied with two synthetic spectra, one for the $M = 3.85$ isentropic core flow temperature of $T = 77$ K, and the other is the horizontal line-of-sight averaged spectrum for the temperature distribution predicted by the 3-D Navier–Stokes code with the Lorentz force and Joule heat turned off (see Fig. 12). One can see that the two synthetic spectra are very close, demonstrating that the contribution of warm boundary layers into the line-of-sight spectrum is insignificant. On the other hand, both synthetic spectra somewhat underpredict the flow temperature, because the tail of the experimental spectrum is higher than that of the synthetic spectra (see Fig. 11). The difference between the measured and the predicted flow temperatures cannot be explained by flow heating by the dc discharge, which is illustrated by Fig. 10, and is also unlikely to be due to heating by the nanosecond pulse discharge, which has estimated upper bound power approximately 4 times lower than the dc discharge (0.24 kW vs 0.9 kW).

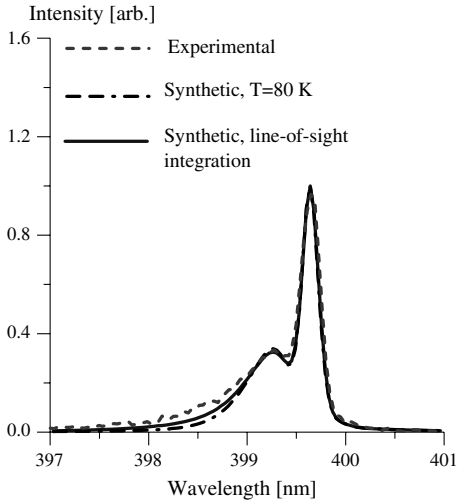

Fig. 11 Comparison of experimental spectrum of Fig. 10 (without dc discharge) and synthetic spectra for $T = 80$ K and for the temperature distribution predicted by the flow code for the horizontal line-of-sight (see Fig. 12).

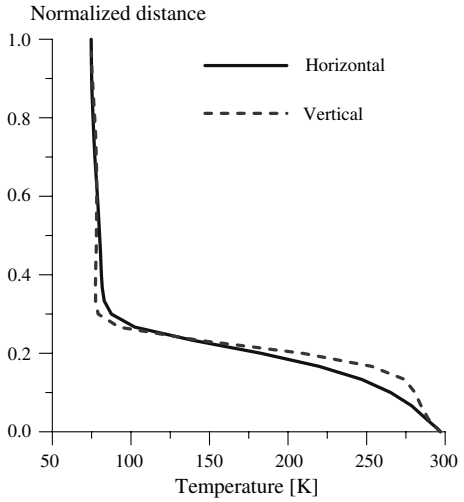

Fig. 12 Static temperature distributions along the horizontal and vertical centerlines in a cold $M = 4$ flow, $x = 16.5$ cm downstream of the nozzle throat (without Joule heating and Lorentz force).

Figure 13 shows normalized test section static pressure traces measured in a $M = 4$ nitrogen flow at the plenum pressure of $P_0 = 600$ torr, with and without Lorentz force applied at the magnetic field of $B = 1.63$ T. As in our previous work [3], static pressure was measured for both accelerating and decelerating Lorentz force directions, each generated by two different combinations of transverse B field and transverse current directions. This was done to isolate the polarity-dependent Lorentz force effect from the polarity-independent Joule heat effect. Turning the pulser on in the presence of magnetic field, without applying transverse dc electric field, i.e., generating ionization in the test section without applying Lorentz force resulted in a static pressure increase by 2–3% from the baseline pressure of 4.8 torr, due to Joule heating generated by the pulser (see Fig. 13). The other four pressure traces plotted in Fig. 13 correspond to four different combinations of transverse current vector and magnetic field vector directions, east/up, west/down (both producing accelerating force, see Fig. 2), west/up, and east/down (both producing retarding force).

As in our previous measurements, the static pressure increased for all four combinations. However, the pressure rise for both accelerating force configurations was higher than for both retarding force configurations (see Fig. 13). Normalized static press for the retarding and for the accelerating Lorentz force was $\Delta P_R/P = 1.19 \pm 0.03$ and $\Delta P_A/P = 1.11 \pm 0.03$, for the same time-averaged dc currents of $\langle I \rangle = 0.93\text{–}0.94$ A, as shown in Fig. 9. The normalized baseline pressure (with no Lorentz force applied) was 1.00 ± 0.03. This effect is consistent with our previous results [3] obtained in $M = 3$ nitrogen and air flows ionized by the CPT pulse generator. Basically, static pressure increases due to Joule heating, which is nearly identical in all four cases (e.g. see Fig. 8). However, flow acceleration by the Lorentz force reduces the pressure rise, while flow deceleration increases it. Note, however, that in spite of the higher flow conductivity achieved in the present work (a factor of 2.5 higher than in $M = 3$ flows, see Fig. 9), the Lorentz force effect on the static pressure is somewhat lower than in our previous work, $(\Delta P_R - \Delta P_A)/P = 0.13$ [3]. From the results of Fig. 13, the effective Joule heating factor (i.e., the discharge energy fraction going into Joule heating of the flow at the present conditions) [3]

$$\alpha \cong \frac{\Delta P_A + \Delta P_R}{2} \frac{M^2 - 1}{(\gamma - 1)M} \frac{a}{j_y E_y L} \tag{11}$$

is $\alpha \approx 0.2$. In Eq. (11), $j_y = 0.093$ A/cm^2 is transverse current density, $E_y = 230$ V/cm is transverse electric field, $L = 4.5$ cm is the length of the MHD section, $M = 3.85$, $\gamma = 1.4$, and $a = 297$ m/s is the speed of sound at $T = 77$ K. At the present experimental conditions, the effective loading parameter, i.e., the ratio of

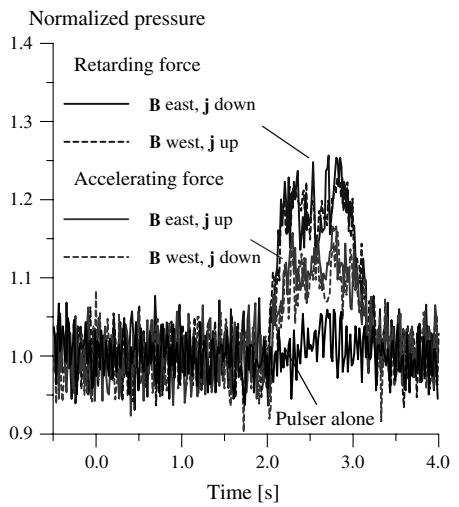

Fig. 13 Typical normalized static pressure traces in a $M = 4$ nitrogen flow at $P_0 = 600$ torr, $P_{test} = 4.8$ torr, $B = 1.63$ T, $\nu = 100$ kHz. $U_{PS} = 1.4$ kV, and $R = 0.5$ kΩ. Lorentz force is applied for 1 sec duration.

Joule heating to the Lorentz force work is $K = \alpha E_y / MaB \approx 4.2$, is nearly the same as in our previous work in $M = 3$ flows, $K \approx 4$.

To verify whether the static pressure change shown in Fig. 13 is indeed caused by the flow acceleration and deceleration by the Lorentz force, we used the 3-D Navier–Stokes/MHD flow code briefly described in Sec. III. In the calculations, experimental values of voltage between dc electrodes, $U_{DC} = 900$ V, magnetic field, $B = 1.5$ T, and effective Joule heating factor, $\alpha = 0.2$, were used. As discussed in Sec. III, the conductivity was adjusted until the calculated current agreed with the experimental value at the same voltage between the dc electrodes, $\sigma = 0.17$ mho/m for $U_{DC} = 900$ V.

Figure 14 shows a contour plot of the Mach number distribution in the center plane of the $M = 4$ nozzle/test section/diffuser, calculated with and without the diffuser section for the baseline conditions, $P_0 = 600$ torr, and without plasmas and magnetic field. It can be seen that the Mach number $M = 3.85$, which is consistent with the number inferred from the static pressure measurements. Two flow separation bubbles formed upstream of the diffuser angle steps, weak compression waves in the test section, and oblique shocks in the diffuser are also visible in Fig. 14.

Figure 15 shows contour plots of axial flow velocity distributions on a crossflow plane at the end of the discharge section for accelerating and decelerating Lorentz force directions, calculated without the diffuser section. In Fig. 15, boundary-layer bulges formed on the plane walls (top and bottom walls in the figure) due to the secondary crossflow are clearly visible. This effect was detected experimentally in our previous work [1], as well as in previous 3-D flow modeling calculations [5,16]. However, the size of the separation bubbles in the new $M = 4$ test section is significantly smaller compared with the $M = 3$ section used in our previous work [1,3]. This occurs primarily because in the new test section the contoured (side) wall width is twice compared with the plane (top/bottom) wall width (as opposed to one half in our previous work [1,13]). Although at the present conditions the difference between the accelerated and decelerated flow fields remains small, it is evident that decelerating force results in a noticeable increase of flow separation bubbles inside the boundary-layer bulges, as well as in thicker boundary layers on the contoured walls (side walls in Fig. 15). The asymmetry of the velocity field in Fig. 15 is caused by the Hall effect.

Figure 16 shows axial distribution of static pressure along the centerline of one of the plane walls, predicted by the code for baseline, accelerated, and decelerated flows (all calculated without the diffuser section), as well as experimental results such as shown in Fig. 13. One can see that static pressures at the end of the MHD section for these three cases, predicted by the code, are in good agreement with the experimental data. In particular, the predicted pressure rise in the flow decelerated by the Lorentz force is greater than the pressure rise in the accelerated flow, by approximately the same amount as measured in the experiment. Normalized static press for the retarding and for the accelerating Lorentz force, predicted by the code, is $\Delta P_R/P = 1.21$ and $\Delta P_A/P = 1.09$, compared with the experimental values of $\Delta P_R/P = 1.20 \pm 0.03$ and $\Delta P_A/P = 1.11 \pm 0.03$, respectively, (see Fig. 13). This result provides further evidence that the static pressure change detected in the present experiments, as well as in our previous work [3], is indeed due to MHD effect.

Figure 17 plots axial velocity for the same three cases as shown in Fig. 16. It can be seen that for the accelerating Lorentz force direction, combination of Joule heating (which decelerates a supersonic flow) and work done by accelerating body force nearly cancel each other and result in a near zero net velocity change. On the other hand, these two effects are combined for the retarding Lorentz force direction, resulting in a velocity reduction by approximately $\Delta u = 25$ m/sec at the end of the MHD section (3.8% velocity reduction). Finally, Fig. 18 shows current vector distribution in the

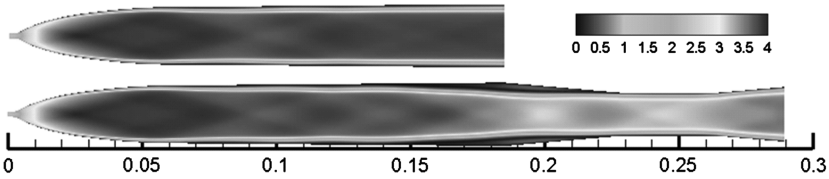

Fig. 14 Center plane Mach number distribution in a baseline $M = 4$ nitrogen flow at $P_0 = 600$ torr, calculated with and without the diffuser. MHD interaction region extends from $x = 0.095$ m to 0.14 m.

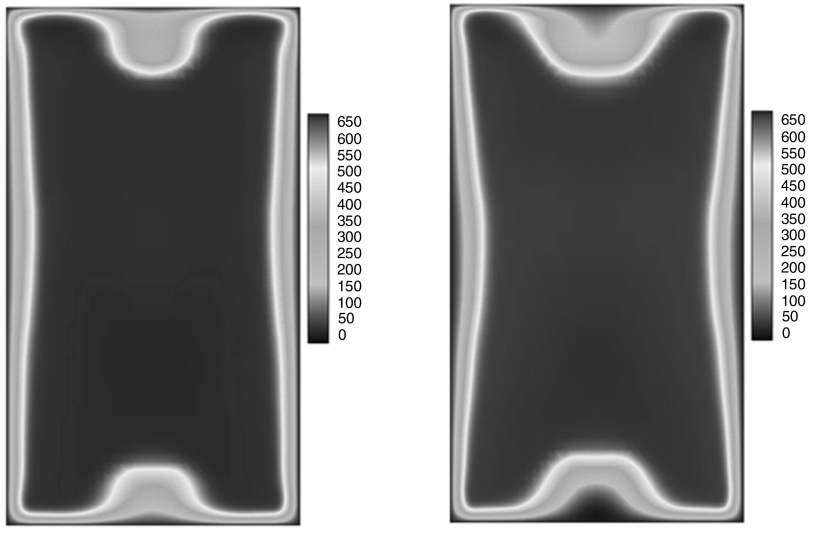

accelerating force retarding force

Fig. 15 Normalized axial velocity distributions at the end of the MHD section ($x = 14$ cm downstream of the nozzle throat) for the accelerated and retarding Lorentz force directions, calculated without the diffuser. Top and bottom walls: plane walls, side walls: contoured walls.

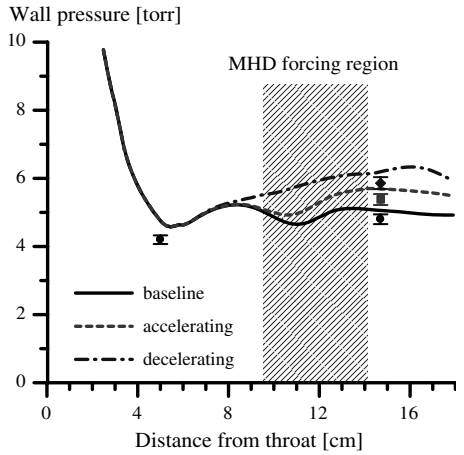

Fig. 16 Static pressure distributions along the centerline of the side (contoured) wall for the baseline, accelerated, and retarded $M = 4$ nitrogen flows, calculated without the diffuser. Location of the pulser-sustainer MHD discharge is shown.

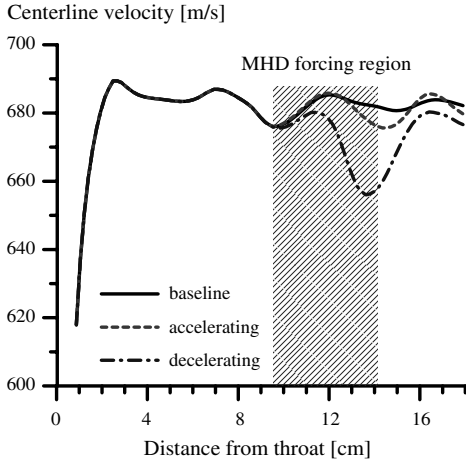

Fig. 17 Centerline axial velocity distributions for the baseline, accelerated, and retarded $M = 4$ nitrogen flows, calculated without the diffuser. Location of the pulser-sustainer MHD discharge is shown.

MHD section for the retarding force direction. It can be seen that there is a significant axial component of the current, caused by the Hall effect, especially near the dc electrodes. The current distribution is consistent with modeling of a crossed pulser-sustainer discharge in transverse magnetic field in quiescent nitrogen, using two-fluid drift-diffusion model of the plasma with the Poisson equation for the electric field [14].

In the present work, the plasma is assumed to be quasi neutral and charge separation in sheaths is neglected. From the current-voltage characteristics of the dc discharge sustained by external pulsed ionization (see Fig. 9), it can be seen that the cathode voltage fall (i.e., sheath voltage) at the present conditions is quite significant, up to 400–500 V. Cathode voltage fall reduces the electric field in the quasi neutral plasma of the discharge positive column. Qualitatively, this results in higher Joule heating and Lorentz force in the cathode sheath, and lower Joule heating and Lorentz force in the positive column. The Hall effect, which is incorporated in the present model, produces a similar result (e.g. see Fig. 18, showing higher current density near the electrodes in the corners of the discharge section). Similar behavior was demonstrated in our previous paper [14], where the structure of the repetitive nanosecond pulser / dc sustainer discharge, including the sheaths, was modeled by solving the Poisson equation coupled with the charged species equations. However, these calculations, which predicted the current distribution consistent with the one predicted in the present work, are computationally very intensive. Coupling a non-quasi-neutral discharge model with the 3-D compressible MHD flow code remains a challenging problem.

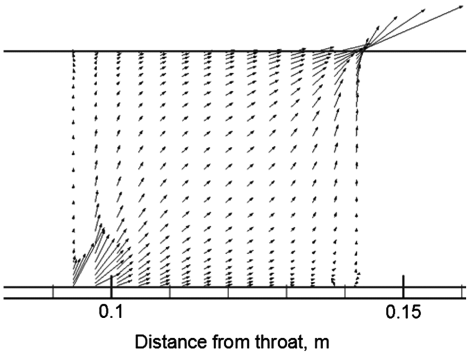

Fig. 18 Current vector distribution for the decelerated $M = 4$ nitrogen flow at the conditions of Figs. 16 and 17.

V. Conclusions

Experiments and numerical simulations are employed to provide insight into the effect of mutually perpendicular magnetic and electric (dc) fields in a cold $M = 4$ flow ionized by high-voltage short duration pulses. The effective flow conductivity is significantly higher than was previously achieved, $\sigma_{\text{eff}} = 0.1$ S/m, at the magnetic field of 1.5–1.6 T. MHD effect on the flow is detected from the flow static pressure measurements. The directions of the electric and magnetic field were selectively reversed to yield two different arrangements each for retarding and acceleration forces. This facilitated understanding of the effects of net flow acceleration and retardation through straightforward pressure measurements. Retarding Lorentz force applied to the flow produces a static pressure increase of 19%, while accelerating force of the same magnitude applied to the same flow results in static pressure increase of 11%. The results of the experiments are compared with modeling calculations using full 3-D Navier–Stokes equations with low magnetic Reynolds number approximation, coupled with the generalized Ohm's law and current continuity equation. The fraction of input discharge power dissipated in the translational/rotational energy mode as Joule heat, used by the model, is estimated from the static pressure measurements. In the calculations, the flow electrical conductivity is adjusted to match the experimental discharge current for the same voltage between the dc electrodes.

The trends in static pressure detected in the experiments were reproduced accurately. The static pressure rise predicted by the code, 20% for the retarding force and 11% for the accelerating force, agrees well with the experimental measurements. Analysis of the calculated results shows that at the present conditions, the accelerating force does not result in a significant velocity change because of the mutually counteracting effects of Joule heating and work done by the Lorentz force. On the other hand, applying the retarding Lorentz force results in an approximately 3.8% flow velocity reduction, by $\Delta u = 25$ m/ sec. These results show that in a cold weakly ionized supersonic flow, an effective ionization process such as high-voltage repetitive pulse ionization, coupled to suitable electric and magnetic fields, can be used for flow deceleration, while acceleration is not achieved because of excessive Joule heating.

Similar results are expected over a fairly wide range of temperatures in nitrogen and dry air flows with external ionization, when vibrational relaxation remains fairly slow. As the temperature is increased, more rapid vibrational relaxation would result in accelerated energy thermalization. This would make the effect of Joule heating on the flow considerably more pronounced compared with the Lorentz force effect, and therefore cause significant net supersonic flow deceleration. At these conditions (at low flow electrical conductivities typical for nonthermal plasmas), isolating the Lorentz force effect would be more difficult. Finally, presence of water vapor in the flow, which also accelerates vibrational relaxation, would produce a similar trend.

Acknowledgments

This work has been supported by the U.S. Air Force Office of Scientific Research grant FA9550-05-1-0085. The authors would like to thank Andrei Starikovskii, Svetlana Starikovskaya (Moscow Institute of Physics and Technology), Patrick Roblin (Electrical and Computer Engineering Department, Ohio State University), and Sergey Gorbatov (A.V. Lykov Heat and Mass Transfer Institute, Minsk, Belarus) for helpful suggestions on nanosecond pulse energy measurement.

References

[1] Nishihara, M., Jiang, N., Rich, J. W., Lempert, W. R., Adamovich, I. V., and Gogineni, S., "Low-Temperature Supersonic Boundary Layer Control Using Repetitively Pulsed Magnetohydrodynamic Forcing," *Physics of Fluids*, Vol. 17, No. 10, 2005, pp. 106102–12. doi:10.1063/1.2084227

[2] Murray, R. C., Zaidi, S. H., Carraro, M. R., Vasilyak, L. M., Macheret, S. O., Shneider, M. N., and Miles, R. B., "Magnetohydrodynamic Power Generation Using Externally Ionized, Cold, Supersonic Air as Working Fluid," *AIAA Journal*, Vol. 44, No. 1, 2006, pp. 119–127. doi:10.2514/1.11611

[3] Nishihara, M., Rich, J. W., Lempert, W. R., Adamovich, I. V., and Gogineni, S., "Low-Temperature $M = 3$ Flow Deceleration by Lorentz Force," *Physics of Fluids*, Vol. 18, No. 8, 2006, pp. 086101–11. doi:10.1063/1.2265011

[4] Kalra, C., Zaidi, S., Shneider, M., and Miles, R., "Shockwave Induced Turbulent Boundary Layer Separation Control with Plasma Actuators," *47th Aerospace Sciences Meeting and Exhibit*, AIAA Paper 2009-1002, Orlando, FL, 5–8 Jan. 2009.

[5] Rawat, P., Zhong, X., Singh, V., and Gogineni, S., "Numerical Simulation of Secondary Flow in a Weakly Ionized Supersonic Flow with Applied Electromagnetic Field," *36th AIAA Plasmadynamics and Lasers Conference*, AIAA Paper 2005-5050, Toronto, Ontario, June 2005.

[6] Yu. P. Raizer, *Gas Discharge Physics*, Springer–Verlag, Berlin, 1991, Chap. 5.

[7] Grekhov, I. V., Korotkov, S. V., Stepaniants, A. L., Khristyuk, D. V., Voronkov, V. B., and Aristov, Y. V., "High-Power Semiconductor-Based Nano and Subnanosecond Pulse Generator with a Low Delay Time," *IEEE Transactions on Plasma Science*, Vol. 33, No. 4, 2005, pp. 1240–1244. doi:10.1109/TPS.2005.852349

[8] Vasilyak, L. M., Kostyuchenko, S. V., Krasnochub, A. V., Kudryavtsev, N. N., and Kurkin, G. A., "An Experimental Investigation of the Electrodynamic and Spectral Characteristics of a Nanosecond Pulse-Periodic Discharge in Chlorine," *High Temperature*, Vol. 33, No. 6, 1995, pp. 822–828.

[9] Rai, V. N., and Shukla, M., "Simple Probes and Attenuators for Measurement of High-Voltage Sub-Nanosecond Pulses," *Measurement Science and Technology*, Vol. 5, No. 11, 1994, pp. 1396–1401. doi:10.1088/0957-0233/5/11/014

[10] Brady, M. M., and Dedrick, K. G., "High-Voltage Pulse Measurement with a Precision Capacitive Voltage Divider," *Review of Scientific Instruments*, Vol. 33, No. 12, 1962, pp. 1421–1428. doi:10.1063/1.1717792

[11] Fowkes, W. R., and Rowe, R. M., "Refinements in Precision Kilovolt Pulse Measurements," *IEEE Transactions on Instrumentation and Measurement*, Vol. 15, No. 4, 1966, pp. 284–292. doi:10.1109/TIM.1966.4313552

[12] Gaitonde, D. V., "A High-Order Implicit Procedure for the 3-D Electric Field in Complex Magnetogasdyanamic Simulations," *Computers and Fluids*, Vol. 33, No. 3, 2004, pp. 345–374. doi:10.1016/j.compfluid.2003.06.001

[13] Gaitonde, D. V., "High-Order Solution Procedure for Three-Dimensional Nonideal Magnetogasdynamics," *AIAA Journal*, Vol. 39, No. 11, 2001, pp. 2111–2120. doi:10.2514/2.1207

[14] Nishihara, M., and Adamovich, I. V., "Numerical Simulation of a Crossed Pulser-Sustainer Discharge in Transverse Magnetic Field," *IEEE Transactions on Plasma Science*, Vol. 35, No. 5, 2007, pp. 1312–1324. doi:10.1109/TPS.2007.906440

[15] Asinovskii, É. I., Vasilyak, L. M., Kirillin, A. V., and Markovets, V. V., "Nanosecond Discharge in a Weakly Ionized Plasma," *High Temperature*, Vol. 13, No. 1, 1975, pp. 32–35.

[16] McMullan, R. J., Lindsey, M. F., Adamovich, I. V., and Nishihara, M., "Experimental Validation of a 3-D Magnetogasdynamic Compressible Navier–Stokes Solver," *35th Plasmadynamics and Lasers Conference*, AIAA Paper 2004-2269, Portland, OR, 29 June–1 July 2004.

L. King
Associate Editor